Letter   Editors' Suggestion

Topological Transformation with Emerging Zero Modes in Multistable Metamaterials for Reprogrammable Flexural Stiffness

Lei Wu and Damiano Pasini[*]

Department of Mechanical Engineering, McGill University, Montreal, Quebec H3A 0C3, Canada

Multistability has been so far exploited to modulate stiffness in mechanical metamaterials under either tension or compression. In this work, we unveil a multistable topological change with emerging zero modes delivering an outstanding reprogrammability of flexural stiffness. Theoretical analysis, experiments, and computations elucidate how the topological change transforms the initially rigid metamaterial into an extremely soft state. Blurring the boundary between structures and mechanisms, this work opens up an avenue for designing reprogrammable matter under flexure.

The design of architected materials with tunable stiffness crossing orders of magnitude has become an emergent topic in the field of mechanical metamaterials. Architectures exhibiting both stiff and soft modes can be reprogrammed to achieve a wide range of properties and functionalities [1], such as energy absorption [2,3], load-bearing capacity [4–6], and shape morphing [7,8]. Exploiting multistability has been so far demonstrated to be effective for reprogramming axial (tension and/or compression) stiffness of metamaterials [9–14]. To date, however, the *in situ* reprogrammability of flexural stiffness in a multistable material has yet to be demonstrated, despite bending being a ubiquitous mechanical mode across length scales [15,16].

A forthright approach for reprogramming flexural stiffness is to redistribute the constituent material about the neutral axis. In this Letter, we follow a bottom-up design strategy (Sec. I of Supplemental Material [17]) and introduce a multistable lattice framework featuring a set of members that can undergo a finite rotation, followed by contact and local rearrangement of their spatial position with respect to the flexural axis. This reconfiguration leads to a topological transformation associated with zero-energy modes, yielding a substantial change in flexural stiffness. We theoretically study the framework reconfiguration and propose a physical model that can replicate the framework behavior. Numerical simulations and experiments are also employed to characterize the topologically induced variation in flexural stiffness. We finally demonstrate that our concept can be extended to design mechanism-based matter incorporating both mobility and rigidity.

Framework topology prior to reconfiguration.—Figure 1(a) shows our planar lattice framework obtained by periodically tessellating a unit cell along the x direction. It consists of infinitely rigid pin-jointed bonds and bodies [black regions in Fig. 1(a)], whose geometry can be defined by $h_i (i = 1, 2, 3)$ and $l_j (j = 1, 2, 3, 4)$, but here simplified to $h_1 = l_1$ and $h_2 = l_2$ for demonstrative purposes. The topology of the lattice framework is defined in physical space and characterized by the numbers of nodes, bonds, zero-energy modes, and states of self-stress [18]. By examining the rank of the equilibrium matrix [19], we observe that the unit cell has only three zero-energy modes ($N_m = 3$), which are rigid-body motions (Sec. II of Supplemental Material [17]). This attests that the primitive cell is kinematically determinate and thus unreconfigurable if its bonds are infinitely rigid. We now relax the infinitely rigid assumption, and admit selected bonds, i.e., CD, BE, BD, CE, and their mirrored parts [Fig. 1(b)] to extend and contract. We represent their axial stiffness with linear elastic springs (k_1 for CD and BE and k_2 for BD and CE) [20], and assume the remaining elements as infinitely rigid bodies [black triangles in Fig. 1(b)]. Upon compression, the deformability of the subframe $BCDE$ enables the rigid triangles to undergo a finite rotation that pushes the unit cell towards its second compatible state [21], hence enabling internal reconfiguration.

Compressed framework.—Under compression, the deformation of the framework is symmetric with respect to the x and y axes, an observation that we use to extract and analyze a quarter of the unit cell [dark yellow region in Fig. 1(b)]. The rigid body $DD'E$ translates in the x direction, whereas ABF undergoes a finite rotation until edges AF and $A'F$ come into contact. At this stage, any further rotation between AF and $A'F$ is disallowed due to the hard contact [Fig. 1(c)]. Assuming all the hinges do not undergo extension or shearing [22,23] and have zero rotational stiffness, we use u_x (the translation of $DD'E$), θ_1 (the rotation
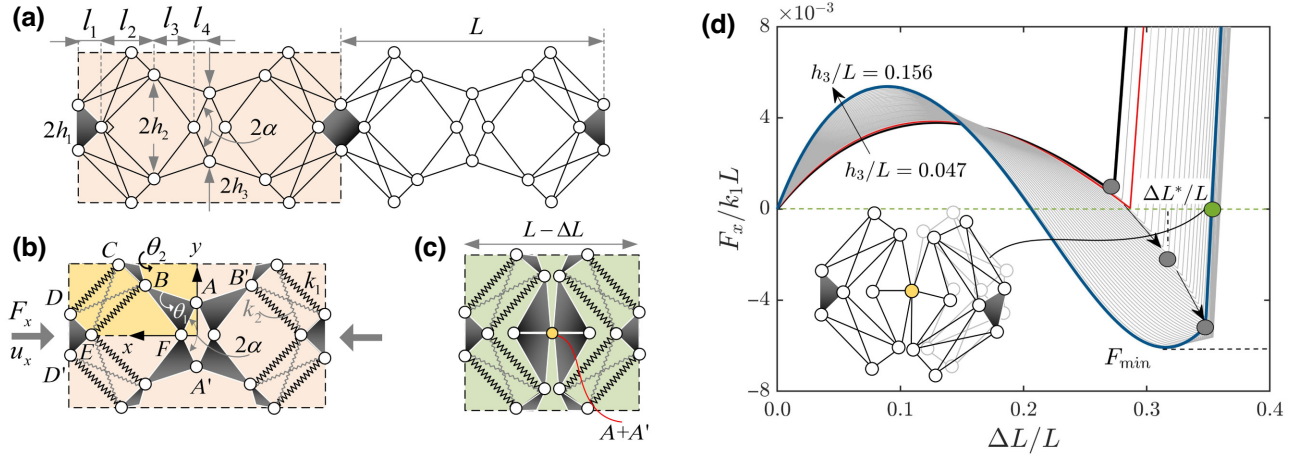
*damiano.pasini@mcgill.ca

FIG. 1. (a) Planar periodic framework with black edges and areas representing infinitely rigid bonds and bodies. Deformable unit cell (b) prior to and (c) post compression. In (c), pairing black triangles are in contact, and hinges A and A' merge into a pivot (yellow spot). (d) Force-displacement curves with $h_1/L = l_1/L = 0.086$, $h_2/L = l_2/L = 0.203$, $h_3/L \in [0.047, 0.156]$, $l_3/L = 0.133$, $l_4/L = 0.078$, $k_1/k_2 = 1$, and $\eta/k_1 L^2 = 6.25 \times 10^{-2}$; gray points indicate establishment of contact; green point represents second stable state; inset shows unit cell in second state (gray) and internal mechanism (black).

of ABF; positive if counterclockwise), and θ_2 (the rotation of BC) to describe the kinematics of the top-left quarter of the unit cell. We write its total potential energy as

$$\Pi = \frac{k_1}{2}(\Delta CD^2 + \Delta BE^2) + \frac{k_2}{2}(\Delta CE^2 + \Delta BD^2)$$
$$+ \eta H(-\theta_1 - \alpha)(\theta_1 + \alpha)^2 - \frac{F_x u_x}{2}, \quad (1)$$

where Δ denotes the extension of the linear springs (CD, BE, BD, and CE), η is a parameter penalizing the relative rotation between AF and $A'F$ when the contact arises, $\alpha = \arctan(h_3/l_4)$, $H(\cdot)$ is the Heaviside function, and $-F_x u_x/2$ is the potential of the external work. Π can be written as $k_1 L^2 \Pi^*$, where Π^* is a nondimensional function of $\eta/k_1 L^2$, k_2/k_1, u_x/L, θ_1/α, θ_2/α, $F_x/k_1 L$, h_i/L, and l_j/L. The governing equations are derived by applying the principle of minimum potential energy and solved by the pseudo-arc-length method [24](Sec. III of Supplemental Material [17]).

Figure 1(d) illustrates the force-contract relation of the unit cell, where $\Delta L = 2u_x$ is the contract in the x direction. A set of responses are plotted for varying h_3/L, all showing smooth snap-through paths until the onset of contact [$\theta_1/\alpha = -1$, $\Delta L = \Delta L^*$; gray points in Fig. 1(d)]. The presence of hard internal contact deflects the equilibrium path and leads to a sudden rise in the incremental stiffness. By varying h_3 and prescribing the other geometry parameters, we can tune α and thus alter the state of contact, i.e., gray point positions in Fig. 1(d). If h_3 is comparably small, e.g., $h_3/L = 0.047$, the contact occurs prior to the unstable configuration of equilibrium [25], a phenomenon that prevents the unit cell from reaching its second stable state [black curve in Fig. 1(d)]. Increasing h_3/L can delay the

establishment of contact, and a critical case is plotted in red in Fig. 1(d), where $F_x(\Delta L^*) = 0$. A further increase of h_3/L results in a bistable unit cell with a greater $\|F_{\min}\|$ [blue curve in Fig. 1(d)], strengthening the robustness of the second stable state.

Framework topology post reconfiguration.—Upon removal of the applied compression, the bistable framework retains its second stable state, which we refer to as the condensed state. Due to the presence of internal contact, there exists self-stress in the bonds, and the pairing edges (AF and AF') and hinges (A and A') merge into a new bond and pivot, respectively [4]. The topological change is now entrapped in the reconfigured lattice [inset in Fig. 1(d)], which has four zero-energy modes ($N_m = 4$) including one internal mechanism, i.e., the rotation around the central pivot. This contact-induced topological change is protected by multistability and accompanied by new zero modes, a phenomenon that is distinct from existing topology-transformable matter that is not mechanically multistable [26,27].

From ideal to physical unit cell.—To better elucidate the topological transformation, we propose a physical model that can replicate the mechanical behavior of the ideal framework, where the ideal joints are replaced with living hinges of size $t_0 = 1$ mm [insets of Fig. 2(a)] and the rectangular subframe $BCDE$ is replaced with a solid beam [Fig. 2(a)]. The solid beam $BCDE$ can achieve equivalent functions to the subframe $BCDE$, i.e., providing firm confinement to the rotating triangles, thus ensuring a robust condensed state. Furthermore, the solid beam has a lower risk of local buckling than the subframe.

Compression of physical unit cell.—Finite element (FE) simulations and experiments are performed to study the compressive response of our physical unit cell, which is
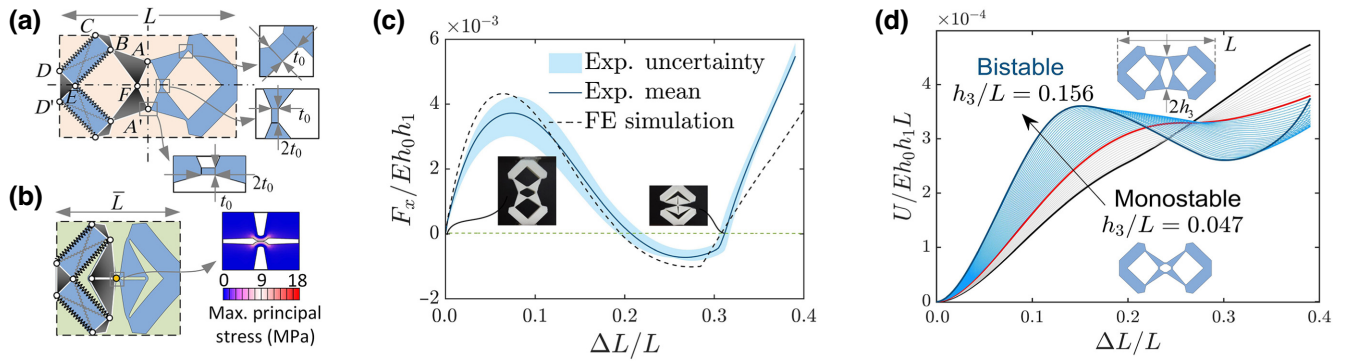
FIG. 2. Physical unit cell in its (a) initial and (b) second stable state (condensed state), where $h_1 = l_1 = 5.5$ mm, $h_2 = l_2 = 13$ mm, $h_3 = 8$ mm, $l_3 = 8.5$ mm, $l_4 = 5$ mm, and $h_0 = 30$ mm; contour plot in (b) illustrates contact-formed pivot and self-stress distribution. (c) Force-displacement curve of unit cell under compression: experiments versus simulations. (d) Evolution of energy landscape for varying h_3/L; gray and blue curves correspond to monostable and bistable unit cells, respectively; red curve ($h_3/L = 0.081$) illustrates regime boundary.

manufactured out of thermoplastic polyurethane [28,29] via fused deposition modeling (Secs. IV and VIII of Supplemental Material [17]). After a cycle of compression and decompression (Supplemental Movie S1 [17]), a bistable unit cell with $h_3/L = 0.125$ and out-of-plane thickness $h_0 = 30$ mm can retain its condensed state with self-stress [Fig. 2(b)], where $\bar{L}$ denotes the length of the reconfigured unit cell. The hinges A and A' are in contact and apparently merged into a newly formed pivot, around which adjacent bodies can rotate. This contact leads to a change in domain connectivity and thus alters the unit cell topology [26]. Figure 2(c) shows a comparison between simulated and tested results in a force-displacement plot. In the linear regime, the curves are aligned, whereas a deviation is observed at the instance of snap-through instability, mainly attributed to fabrication imperfections emerging in the small-size hinges [30]. Overall, the experimental and numerical curves are aligned with the results of our framework model and show a turning point at $\Delta L/L \approx 0.3$ with an abrupt change in incremental stiffness due to the topology change induced by the internal contact.

A key parameter governing the topological reconfigurability of the unit cell is h_3/L. To fully explore its role, we now investigate the energy landscape and plot in Fig. 2(d) the strain energy normalized by $Eh_0 h_1 L$, where $E = 146$ MPa is the linear Young's modulus of the base material (Sec. IX of Supplemental Material [17]). A unit cell with $h_3/L = 0.047$ is monostable and thus unable to maintain the reconfigured shape upon load removal (black curve). On the other hand, increasing h_3/L delays the initiation of contact and results in a double-well energy landscape (blue curves). The critical value of h_3/L, beyond which the unit cell is bistable, is 0.081 (red curve). These insights prompt us to consider bistable unit cells and investigate the role of topological transformation in their flexural stiffness.

Flexural stiffness of physical unit cell prior to reconfiguration.—To study the flexural stiffness of a bistable unit cell before reconfiguration (D_{stiff}), we apply at the unit cell boundaries a pair of moments (M_z) that generate a relative rotation angle of ϕ [left inset in Fig. 3]. Under small deformation, D_{stiff} can be approximated as $M_z L/\phi$, and its value can also be experimentally measured through a four-point bending test (Sec. VI of Supplemental Material [17]). The purple curve in Fig. 3 shows a positive correlation between D_{stiff} and h_3/L. In particular, a unit cell with $h_3/L = 0.156$ has a flexural stiffness 1.76 times that of a unit cell with $h_3/L = 0.089$. To gain more insights, we develop a discretized theoretical model to predict D_{stiff} (Sec. V of Supplemental Material [17]), where we take into account the deformation of the hinges [31,32] and triangle ABF [33]. The results from the discretized model show that under infinitesimal bending, the strain energy contribution of the hinges is much lower than that of both the solid beam $BCDE$ and triangle ABF, which act as load-bearing elements for the unit cell prior to reconfiguration. Moreover, as h_3/L increases, the strain energy distributes more evenly within the load-bearing elements, making a more efficient use of the base material [34], thus leading to a higher D_{stiff}.

Flexural stiffness of physical unit cell post reconfiguration.—Once topologically reconfigured, the unit cell is condensed in an extremely soft state, where the newly contact-formed pivot (right inset in Fig. 3) becomes the load-bearing element. Its flexural stiffness (D_{soft}) is given by $k_r \bar{L}$, where k_r is the rotation stiffness of the central pivot. We measure k_r in an experiment where the self-weight of the unit cell associated with a mass load is the driving input (Sec. VII of Supplemental Material [17]) [35]. As opposed to D_{stiff}, D_{soft} is almost constant over a range of h_3/L (blue curve in Fig. 3), signifying that k_r is not dependent on the
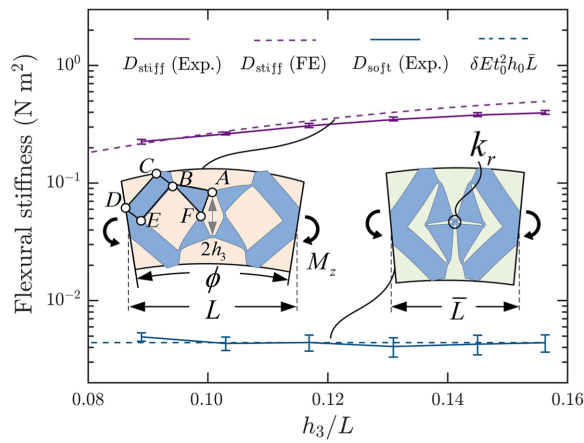
FIG. 3. Flexural stiffness of unit cell ($h_0 = 15$ mm) in its initial (D_{stiff}) and condensed (D_{soft}) state as a function of h_3/L. Two insets illustrate stiff (left) and flexural (right) modes of a unit cell. Experimental results are slightly below those from FE simulations due to the out-of-plane flexure of the specimens.

initial position of the hinges A and A'. k_r can be approximated as $\delta E t_0^2 h_0$, where δ is a parameter characterizing the geometry of the hinge [22]. This is shown by the dashed blue line in Fig. 3, where δ is 0.046, a value accounting for the shape distortion and self-stress of the central pivot. Overall, Fig. 3 demonstrates the substantial change (over an order of magnitude) in flexural stiffness that the topological reconfiguration imparts to the unit cell. This reflects the reallocation of load-bearing elements, from the solid beam $BCDE$ and triangle ABF (deployed state) to the contact-formed pivot (condensed state).

Three-point bending of finite-period tessellations.—We now examine two representative finite-period tessellations ($h_3/L = 0.089$ and 0.156) and perform three-point bending tests [Figs. 4(a)–4(c)]. The average slope of the force-deflection curve is here defined as the deflection stiffness. Each specimen can attain two antagonist modes of deformation (stiff and extremely soft). Before reconfiguration, the deflection stiffness is sizeable for both specimens.

The one with $h_3/L = 0.156$ has an average stiffness 1.72 times that with $h_3/L = 0.089$ [Fig. 4(d)]. Post reconfiguration, both specimens become extremely soft and have comparable stiffness [Fig. 4(e)], as opposed to the pre-reconfiguration state where a change in h_3/L does alter stiffness. This result attests that D_{soft} is mainly governed by the size of the contact-formed pivot, and the role of the initial configuration is negligible. Overall, for the specimen with $h_3/L = 0.156$, the initial deflection stiffness of 1.27 N/mm drops to 0.11 N/mm due to reconfiguration, demonstrating a transition from a rigid structure to an extremely soft mechanism (Supplemental Movie S2 [17]).

Generalization to curved beams.—We showcase here the potential of topological reconfiguration in curved beams. We generate a curved planar lattice by rotating the unit cell's symmetry axis (red dash) with respect to hinge A by τ, and then finding a point, A^*, along the new symmetry axis (black dash), such that $A'F = A^*F$ [Fig. 4(f)]. This operation ensures that in the condensed state, A^* and A get in contact and form a central pivot. Figure 4(g) shows an arc stacked with six curved unit cells ($\tau = \pi/12$) and loaded under a mass of 100 g. Before reconfiguration, the arc is rigid and can barely deform, as opposed to its post reconfigured state, which visibly deflects. The curved concept can be extended to generate a closed framework such as the ring in Fig. 4(h). Here, there is still a dual response: stiff in the deployed state and soft once collapsed, a behavior that has potential application in wearable devices (Supplemental Movie S3 [17]).

Application to mechanism-based matter.—Our unit cell can be used as a bistable hinge to incorporate both mobility and rigidity in mechanism-based metamaterials. Figure 5 shows an example of a panel consisting of an array of rigid squares connected via our unit cells. When all the hinges are inactive (initial state), the whole assembly behaves as a rigid plate resisting flexure [Fig. 5(a)]. In contrast, if all the hinges are activated (condensed state), the panel transitions to a mechanism that can flex with low energy cost [Fig. 5(b)]. If only a portion of the hinges have been activated, the panel is able to show
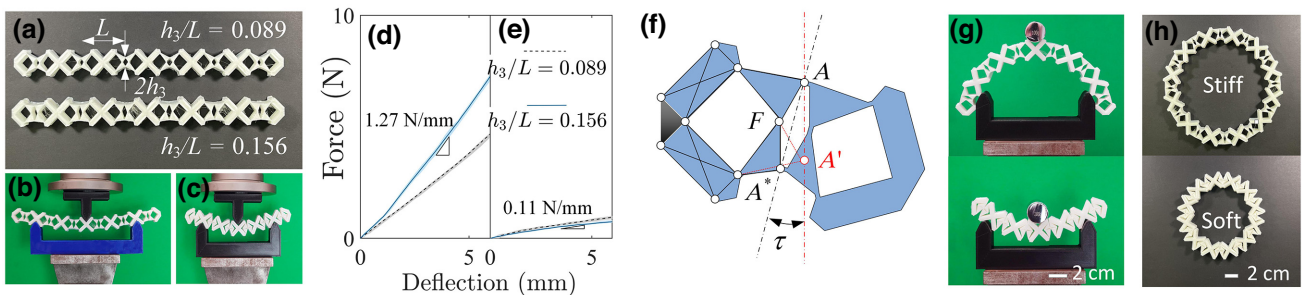

FIG. 4. (a) Finite-period tessellations with $h_3/L = 0.089$ and 0.156. Three-point bending tests (b) prior to and (c) post reconfiguration. Force-deflection responses (d) prior to and (e) post reconfiguration. (f) Geometric operation for generating a curved unit cell. (g) Curved beam lifting a weight of 100 g. (h) Reconfigurable ring capable of switching between stiff and soft modes.
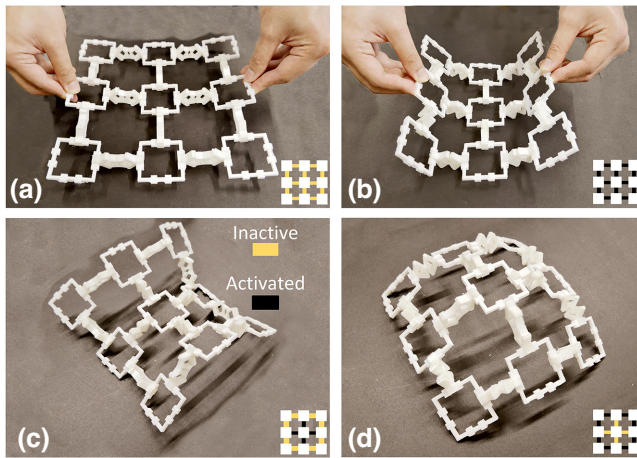
FIG. 5. Representative states of a reprogrammable foldable panel. Black indicates activated hinges, as opposed to yellow (inactive). (a) Stiff mode of the panel acting as a structural plate. (b) Soft mode enabling surface flexure as in a mechanism. States with (c) negative and (d) positive Gaussian curvature obtained by selectively activating hinges.

negative [Fig. 5(c)] or positive [Fig. 5(d)] Gaussian curvature [36,37]. Our bistable hinge can also be embedded into conventional mechanism-based matter, e.g., kirigami or origami, to enrich the mechanical responses beyond existing functionalities.

Conclusions.—We report a multistable metamaterial that leverages a topological reconfiguration to modulate flexural stiffness over an order of magnitude. We first theoretically unveil the emergence of zero-energy modes in the reconfigured lattice, followed by validating numerical and experimental analyses. All results attest to the key role of topological transformation, first enabled by internal rotation and contact, and then robustly preserved through multistability. Our concept can switch its topology *in situ* offering bending stiffness and flexural modes on demand, paving the way to the flexural design of reprogrammable matter across length scales [20,26].

[1] A. Pal, V. Restrepo, D. Goswami, and R. V. Martinez, Exploiting mechanical instabilities in soft robotics: control, sensing, and actuation, Adv. Mater. **33**, 2006939 (2021).

[2] H. Yasuda and J. Yang, Reentrant Origami-Based Metamaterials with Negative Poisson's Ratio and Bistability, Phys. Rev. Lett. **114**, 185502 (2015).

[3] S. Li, H. Fang, and K. W. Wang, Recoverable and Programmable Collapse from Folding Pressurized Origami Cellular Solids, Phys. Rev. Lett. **117**, 114301 (2016).

[4] A. Jamalimehr, M. Mirzajanzadeh, A. Akbarzadeh, and D. Pasini, Rigidly flat-foldable class of lockable origami-inspired metamaterials with topological stiff states, Nat. Commun. **13**, 1 (2022).

[5] Y. Wang, L. Li, D. Hofmann, J. E. Andrade, and C. Daraio, Structured fabrics with tunable mechanical properties, Nature **596**, 238 (2021).

[6] J. A. Jackson, M. C. Messner, N. A. Dudukovic, W. L. Smith, L. Bekker, B. Moran, A. M. Golobic, A. J. Pascall, E. B. Duoss, and K. J. Loh, *et al.*, Field responsive mechanical metamaterials, Sci. Adv. **4**, eaau6419 (2018).

[7] M. Czajkowski, C. Coulais, M. van Hecke, and D. Rocklin, Conformal elasticity of mechanism-based metamaterials, Nat. Commun. **13**, 1 (2022).

[8] C. Coulais, E. Teomy, K. De Reus, Y. Shokef, and M. Van Hecke, Combinatorial design of textured mechanical metamaterials, Nature **535**, 529 (2016).

[9] Y. Chi, Y. Li, Y. Zhao, Y. Hong, Y. Tang, and J. Yin, Bistable and multistable actuators for soft robots: Structures, materials, and functionalities, Adv. Mater. **34**, 2110384 (2022).

[10] J. L. Silverberg, A. A. Evans, L. McLeod, R. C. Hayward, T. Hull, C. D. Santangelo, and I. Cohen, Using origami design principles to fold reprogrammable mechanical metamaterials, Science **345**, 647 (2014).

[11] N. Singh and M. van Hecke, Design of Pseudo-Mechanisms and Multistable Units for Mechanical Metamaterials, Phys. Rev. Lett. **126**, 248002 (2021).

[12] J. Qi, Z. Chen, P. Jiang, W. Hu, Y. Wang, Z. Zhao, X. Cao, S. Zhang, R. Tao, and Y. Li, *et al.*, Recent progress in active mechanical metamaterials and construction principles, Adv. Sci. **9**, 2102662 (2022).

[13] T. Chen, M. Pauly, and P. M. Reis, A reprogrammable mechanical metamaterial with stable memory, Nature **589**, 386 (2021).

[14] Y. Yang, M. A. Dias, and D. P. Holmes, Multistable kirigami for tunable architected materials, Phys. Rev. Mater. **2**, 110601(R) (2018).

[15] D. B. Zhang, E. Akatyeva, and T. Dumitrică, Bending Ultrathin Graphene at the Margins of Continuum Mechanics, Phys. Rev. Lett. **106**, 255503 (2011).

[16] J. F. Fleming and E. A. Egeseli, Dynamic behaviour of a cable-stayed bridge, Earthq. Eng. Struct. Dyn. **8**, 1 (1980).

[17] See Supplemental Material at http://link.aps.org/supplemental/10.1103/PhysRevApplied.19.L061001 for more details of the lattice framework design, theoretical analysis, numerical simulations, sample fabrications, bending stiffness tests, and three video demonstrations.

[18] V. Deshpande, M. Ashby, and N. Fleck, Foam topology: Bending versus stretching dominated architectures, Acta Mater. **49**, 1035 (2001).

[19] S. Pellegrino and C. R. Calladine, Matrix analysis of statically and kinematically indeterminate frameworks, Int. J. Solids Struct. **22**, 409 (1986).

[20] J. Z. Kim, Z. Lu, S. H. Strogatz, and D. S. Bassett, Conformational control of mechanical networks, Nat. Phys. **15**, 714 (2019).

[21] D. Melancon, B. Gorissen, C. J. García-Mora, C. Hoberman, and K. Bertoldi, Multistable inflatable origami structures at the metre scale, Nature **592**, 545 (2021).

[22] Z. Meng, W. Chen, T. Mei, Y. Lai, Y. Li, and C. Chen, Bistability-based foldable origami mechanical logic gates, Extreme Mech. Lett. **43**, 101180 (2021).

[23] J. N. Grima and K. E. Evans, Auxetic behavior from rotating squares, J. Mater. Sci. Lett. **19**, 1563 (2000).

[24] E. Doedel, H. B. Keller, and J. P. Kernevez, Numerical analysis and control of bifurcation problems (I): Bifurcation in finite dimensions, Int. J. Bifurcation Chaos **1**, 493 (1991).

[25] K. Che, C. Yuan, J. Wu, H. Jerry Qi, and J. Meaud, Three-dimensional-printed multistable mechanical metamaterials with a deterministic deformation sequence, J. Appl. Mech. 84 (2017).

[26] C. Coulais, A. Sabbadini, F. Vink, and M. van Hecke, Multi-step self-guided pathways for shape-changing metamaterials, Nature **561**, 512 (2018).

[27] S. Li, B. Deng, A. Grinthal, A. Schneider-Yamamura, J. Kang, R. S. Martens, C. T. Zhang, J. Li, S. Yu, and K. Bertoldi, *et al.*, Liquid-induced topological transformations of cellular microstructures, Nature **592**, 386 (2021).

[28] B. Chen, L. Chen, B. Du, H. Liu, W. Li, and D. Fang, Novel multifunctional negative stiffness mechanical metamaterial structure: Tailored functions of multi-stable and compressive mono-stable, Compos. Part B: Eng. **204**, 108501 (2021).

[29] S. Sato, T. Yamaguchi, K. Shibata, T. Nishi, K. Moriyasu, K. Harano, and K. Hokkirigawa, Dry sliding friction and wear behavior of thermoplastic polyurethane against abrasive paper, Biotribology **23**, 100130 (2020).

[30] In the linear regime, the compression stiffness of the unit cell is mostly governed by the characteristics of the solid beam *BCDE*, which is less sensitive to defects. In the snap-through regime, the rotation of the hinge dominates the stiffness of the unit cell, and thus defects have a more sizeable impact.

[31] C. Coulais, C. Kettenis, and M. van Hecke, A characteristic length scale causes anomalous size effects and boundary programmability in mechanical metamaterials, Nat. Phys. **14**, 40 (2018).

[32] B. Deng, C. Mo, V. Tournat, K. Bertoldi, and J. R. Raney, Focusing and Mode Separation of Elastic Vector Solitons in a 2D Soft Mechanical Metamaterial, Phys. Rev. Lett. **123**, 024101 (2019).

[33] E. Filipov, K. Liu, T. Tachi, M. Schenk, and G. H. Paulino, Bar and hinge models for scalable analysis of origami, Int. J. Solids Struct. **124**, 26 (2017).

[34] J. Berger, H. Wadley, and R. McMeeking, Mechanical metamaterials at the theoretical limit of isotropic elastic stiffness, Nature **543**, 533 (2017).

[35] B. Shrimali, M. Pezzulla, S. Poincloux, P. M. Reis, and O. Lopez-Pamies, The remarkable bending properties of perforated plates, J. Mech. Phys. Solids **154**, 104514 (2021).

[36] T. Chen, J. Mueller, and K. Shea, Integrated design and simulation of tunable, multi-state structures fabricated monolithically with multi-material 3D printing, Sci. Rep. **7**, 1 (2017).

[37] J. A. Faber, J. P. Udani, K. S. Riley, A. R. Studart, and A. F. Arrieta, Dome-patterned metamaterial sheets, Adv. Sci. **7**, 2001955 (2020).